A Reactive Manganese(IV)-Hydroxide Complex: A Missing Intermediate in Hydrogen Atom Transfer by High-Valent Metal-Oxo Porphyrinoid Compounds

Jan Paulo T. Zaragoza, **Maxime A. Siegler**, and **David P. Goldberg**[*]

Department of Chemistry, The Johns Hopkins University, 3400 N. Charles Street, Baltimore, MD 21218, United States

Abstract

High-valent metal-hydroxide species are invoked as critical intermediates in both catalytic, metal-mediated O_2 activation (e.g. by Fe porphyrin in Cytochrome P450) and O_2 production (e.g. by the Mn cluster in Photosystem II). However, well-characterized mononuclear $M^{IV}(OH)$ complexes remain a rarity. Herein we describe the synthesis of $Mn^{IV}(OH)(ttppc)$ (**3**) (ttppc = tris(2,4,6-triphenylphenyl) corrole), which has been characterized by X-ray diffraction (XRD). The large steric encumbrance of the ttppc ligand allowed for isolation of **3**. The complexes $Mn^V(O)(ttppc)$ (**4**) and $Mn^{III}(H_2O)(ttppc)$ (**1**•H_2O) were also synthesized and structurally characterized, providing a series of Mn complexes related only by the transfer of hydrogen atoms. Both **3** and **4** abstract an H atom from the O–H bond of 2,4-di-tert-butylphenol (2,4-DTBP) to give a radical coupling product in good yield (**3** = 90(2)%, **4** = 91(5)%). Complex **3** reacts with 2,4-DTBP with a rate constant of $k_2 = 2.73(12) \times 10^4$ M^{-1} s^{-1}, which is ~3 orders of magnitude larger than **4** ($k_2 = 17.4(1)$ M^{-1} s^{-1}). Reaction of **3** with a series of para-substituted 2,6-di-tert-butylphenol derivatives (4-X-2,6-DTBP; X = OMe, Me, tBu, H) gives rate constants in the range $k_2 = 510(10) - 36(1.4)$ $M^{-1}s^{-1}$ and led to Hammett and Marcus plot correlations. Together with kinetic isotope effect measurements, it is concluded that O–H cleavage occurs by a concerted H-atom transfer (HAT) mechanism, and that the $Mn^{IV}(OH)$ complex is a much more powerful H-atom abstractor than the higher-valent $Mn^V(O)$ complex, or even some $Fe^{IV}(O)$ complexes.

INTRODUCTION

Terminal, high-valent, metal-hydroxide ($M^{n+}(OH)$) complexes (n ≥ 3) with first row transition transition metals are relatively rare, in part because of their tendency to form hydroxo- or oxo-bridged (M-O(H)-M) structures. Redox instability, especially for the

[*]**Corresponding Author** dpg@jhu.edu.

Notes

ASSOCIATED CONTENT

Supporting Information. The Supporting Information is available free of charge via the Internet at http://pubs.acs.org.

Kinetics studies, UV-vis, ^{1}H NMR, and X-band EPR spectra, Magnetic susceptibility measurements, GC-FID traces and parameters, Single-crystal X-ray crystallography analysis and data, summary of selected bond lengths, coordinates of the DFT-optimized structures.

tetravalent (n = 4) species, is also a significant destabilizing factor, leading to reduction or disproportionation of the desired metal(IV) complex.[1–4] In contrast, the synthesis and isolation of related high-valent, metal-oxo ($M^{n+}(O)$) species has been more successful.[5–9] However, both heme and nonheme $M^{n+}(OH)$ species have emerged recently as desirable targets, with some limited successes being reported.[10–14] Studies involving $Fe^{III}(OH)$ complexes have examined their reactivity in H-atom transfer (HAT) or proton-coupled electron-transfer (PCET) reactions.[11–13, 15] Similarly, a few terminal $Mn^{III}(OH)$ complexes have been prepared, and their reactivity toward HAT investigated.[16–18] However, Fe(OH) and Mn(OH) complexes with formal oxidation states greater than +3 are exceedingly rare. The first Fe(OH) complex outside of a protein[19] at the formal +4 oxidation level was recently reported by our laboratory.[20] The first report of an isolated $Mn^{IV}(OH)$ complex came from Busch in 2006, which described a nonheme Mn^{IV} complex with two terminal OH ligands.[21] Since 2006, only two examples of isolated monohyrodroxo-Mn^{IV} complexes have been reported, one from Borovik[10] and the other from Fujii,[22] and both were prepared with nonheme ligands (Chart 1).

The interest in high-valent, terminal, hydroxometal species comes from their central roles in biological and synthetic catalytic processes. One key role is in the oxidation of C-H substrates. Homolytic cleavage of C-H bonds by high-valent metal-oxo species ($M^n(O)$) is an essential step in the functionalization of organic molecules mediated by enzymes and synthetic catalysts, and leads to $M^{n-1}(OH)$ and carbon radical (R•) intermediates. The fate of the metal-hydroxide determines the ultimate outcome of these reactions. Typically, R• recombines with the metal-bound OH moiety to give a hydroxylated (ROH) product. The heme monooxygenase Cytochrome P450 (CYP) provides a well-established example of this hydroxylation pathway (Scheme 1).[23–28] However, deviations from this mechanistic scenario occur, originating from the divergent reactivity of $Fe^{IV}(OH)(porph)(cys)$ (protonated "Compound II"). In certain CYPs, $Fe^{IV}(OH)(porph)(cys)$ can react as an H-atom abstractor, resulting in desaturation of the substrate, as opposed to hydroxylation.[29–31] The CYP enzyme known as OleT from *Jeotgalicoccus sp.*, provides a fascinating example of the latter chemistry, in which desaturation of long chain fatty acid substrates leads to C-C bond cleavage and production of terminal alkenes, as opposed to C-H hydroxylation.[32–33] The latter reactivity has potential consequences for the development of biofuel.[34–35] A mononuclear, terminal iron-hydroxide also plays a similarly important role in the nonheme iron enzyme soybean lipoxygenase (SLO). An $Fe^{III}(OH)$ in SLO abstracts an H-atom from the bis-allylic C-H bond of linoleic acid substrates. The details of this process, and especially the observation of gigantic kinetic isotope effects (KIEs) for C-H cleavage by the $Fe^{III}(OH)$ intermediate, have been the focus of several studies.[36–38]

The reverse reaction, in which an $M^{n+}(OH)$ species releases a net H•, may play an important role in the water oxidation process carried out by the Mn-containing oxygen-evolving cluster (OEC) in photosystem II.[39–42] Proposed mechanisms for this process involve the sequential oxidation and deprotonation of a $Mn^{III}(H_2O)$ species, to give $Mn^{IV}(OH)$ and ultimately $Mn^V(O)$ species (Scheme 1). The latter species may then facilitate O–O bond formation leading to O_2 production. However, despite much effort to unravel the mysteries of Mn-mediated water oxidation, many questions remain about the mechanism, and possible role(s), of $Mn^{IV}(OH)$ and $Mn^V(O)$ intermediates. Synthetic analogs of the Mn cluster allow

for detailed correlations to be made between geometric and electronic structure, and the reactivity of Mn-bound H_2O/OH/O species. These studies in turn have provided information to help delineate plausible water oxidation scenarios for the OEC.[43–51]

Of the few $Mn^{IV}(OH)_n$ (n =1, 2) complexes that are known[10, 21–22, 52–53] (Chart 1), there are no examples of crystallographically characterized monohydroxo complexes.[54] Previously, we reported the generation of a metastable Mn^{IV}(OH) corrolazine complex,[55] but were unsuccessful in growing crystals of this complex for characterization by X-ray diffraction (XRD), and a detailed study of the reactivity of this complex was not performed. Herein we report the synthesis and crystal structure of Mn^{IV}(OH)(ttppc), which, to our knowledge, is the first Mn^{IV}(OH) complex characterized by single crystal XRD. The related Mn^V(O) and $Mn^{III}(H_2O)$ ttppc complexes were also synthesized and characterized by XRD, demonstrating the versatility of the ttppc ligand to house $Mn^{n+}(OH_x)$ (n = 3 – 5; x = 2, 1, 0) species in three different oxidation and protonation states in an identical porphyrinoid ligand environment. The reactivity of the Mn^{IV}(OH) complex in HAT reactions with O-H substrates was examined, and it was found to exhibit dramatically enhanced rates of HAT as compared to its higher oxidation state Mn^V(O) relative. Hammett and Marcus analyses, together with kinetic isotope effects, provide detailed insight into the mechanism of HAT for these Mn^{IV}(OH) and Mn^V(O) complexes.

RESULTS AND DISCUSSION

Synthesis and Structural Characterization of Mn^IV(OH)(ttppc).

Our previous synthesis of Fe^{IV}(OH)(ttppc)[20] suggested that the analogous Mn^{IV}(OH)(ttppc) could be prepared by the same method involving ligand metathesis of a metal-chloride precursor. The $ttppcH_3$ ligand was metalated with $Mn(OAc)_2$ to give Mn^{III}(ttppc) (**1**) in 88% yield according to a literature method.[56] Aerobic oxidation of dark green **1** in dichloromethane in the presence of excess $HCl_{(aq)}$ led to formation of brown Mn^{IV}(Cl)(ttppc) (**2**), which was monitored by UV-vis spectroscopy. After work-up, the crude reaction mixture was purified by column chromatography to yield **2** as a brown solid (40% yield). Single crystals of **2** were obtained from CH_2Cl_2/*n*-pentane, and the structure is shown in Figure 1. The structure reveals a 5-coordinate Mn with an axial Cl⁻ ligand, and charge balance requires a formal +4 oxidation state at Mn. The Mn^{IV}–Cl distance of 2.2754(11) Å is similar to other Mn^{IV}(Cl) corroles.[57–58] This complex served as starting material for preparation of the target Mn^{IV}(OH) species.

Titration of the chloride complex **2** with Bu_4NOH (0 – 1.5 equiv) in toluene/CH_3CN (100:1) at 23 °C was followed by UV-vis spectroscopy (Figure 2). Isosbestic conversion of **2** to a new species with λ_{max} = 420, 553, 670 nm was observed upon addition of 1 equiv of OH⁻, after which no further changes in spectral features were seen. This reaction was also followed by EPR spectroscopy, as seen in the inset of Figure 2. The X-band EPR spectrum of **2** at 12 K reveals a well-resolved axial spectrum with g = 4.1, 2.0 and $A(^{55}Mn)_{ave}$ = 84, 60 MHz, which can be assigned to a high-spin Mn^{IV} (d^3, S = 3/2) complex. Addition of Bu_4NOH leads only to a broadening of the g_1 signal near 4.1, displaying surprisingly little change for a change in the first coordination sphere of the Mn ion. However, other Mn^{IV}

complexes have exhibited EPR spectra that are similarly insensitive to the identity of the axial ligand.[22, 59–60]

The UV-vis and EPR titrations suggested that the chloride ligand in **2** could be quantitatively displaced by hydroxide. Following the two-phase synthesis of $Fe^{IV}(OH)(ttppc)$,[20] the Mn(OH) complex was prepared on a bulk scale by the addition of aqueous LiOH to a toluene solution of **2**. Recrystallization from toluene/*n*-pentane yielded brown crystals of $Mn^{IV}(OH)(ttppc)$ (**3**), which were analyzed by single crystal X-ray diffraction (XRD).

The structure of **3** (Figure 3) shows the axial chloride ligand of **2** has been replaced by hydroxide, as expected. While the hydrogen atom of the OH^- group in **3** could not be accurately located from the difference Fourier maps due to the disorder of the Mn–OH unit, charge balance and the Mn-O bond distance are consistent with the presence of an axial OH^- ligand. The Mn-O bond distance (from the major component of the disorder) for the terminal hydroxide ligand in **3** is 1.881(2) Å, which is slightly longer than those reported for the few other $Mn^{IV}(OH)_n$ (n = 1, 2) complexes (1.793(2) – 1.830(4) Å),[10, 21–22, 52–53] but much longer than a typical $Mn^{IV}(O)$ distance (1.58 – 1.71 Å).[22, 61–64] The Mn-O distance in **3** is quite close to that seen for $Fe^{IV}(OH)(ttppc)$ (Fe–O = 1.857(3) Å).[20]

The UV-vis and X-band EPR spectra (Figure S1) of crystalline **3** match those seen in the spectral titrations in Figure 2. The structural and spectroscopic data confirm that **3** is a rare example of a terminal $Mn^{IV}(OH)$ complex, and is the first example, to our knowledge, of a monomeric $Mn^{IV}(OH)$ complex characterized by X-ray crystallography.

Synthesis and Structural Characterization of $Mn^{V}(O)(ttppc)$.

Corroles and corrolazines are known to stabilize high-valent $Mn^{V}(O)$ complexes. The first crystal structure of an $Mn^{V}(O)$ porphyrinoid complex was obtained with an octaaryl-substituted corrolazine.[65] The *in situ* generation of $Mn^{V}(O)(ttppc)$ was described previously, and it was shown to mediate oxygen atom transfer to alkene substrates.[56] However, this complex was not isolated as a pure solid, and no structural information was obtained.

We set out to crystallize $Mn^{V}(O)(ttppc)$ and definitively characterize the structure of this complex by single crystal XRD. The synthesis of $Mn^{V}(O)(ttppc)$ (**4**) followed the earlier report from Chang, with minor modifications.[56] The original method involved the addition of iodosylbenzene (PhIO) to $Mn^{III}(ttppc)$ in CH_2Cl_2, followed by flash chromatography on basic alumina. However, the resulting $Mn^{V}(O)$ complex was only metastable in CH_2Cl_2 at 23 °C ($t_{1/2}$ ~7 h). We examined other solvents for the synthesis and purification of **4** in order to improve stability. Performing the PhIO oxidation and purification on basic alumina in ethyl acetate resulted in much better stability, with **4** showing little or no decay in this solvent for weeks at 23 °C. Vapor diffusion of *n*-pentane into a concentrated solution of **4** in ethyl acetate led to the growth of dark-red blocks after a few days. Crystals of **4** suitable for X-ray structure determination were obtained from ethyl acetate/*n*-pentane, and the structure of **4** is shown in Figure 4.

The structure of **4** revealed a five-coordinate Mn ion, with $Mn-N_{pyrrole}$ distances between 1.8970(12) – 1.9249(11) Å, and an apparent Mn–O bond distance of 1.6332(16) Å. This

Mn–O distance is significantly longer than that seen for $Mn^V(O)$ corrolazine (1.5455(18) Å),[65] or for other nonheme $Mn^V(O)$ complexes (1.548(4) – 1.558(4) Å).[66–68] This elongated Mn-O bond could possibly be consistent with a high-spin $Mn^V(O)$ complex ($S = 1$) based on the DFT-optimized geometries of excited state ($S = 1$) $Mn^V(O)$ corroles and corrolazines,[69] although all of the former $Mn^V(O)$ species were characterized experimentally as exhibiting low-spin ($S = 0$) ground states. Crystals of **4** dissolved in benzene-d_6 gave a sharp, diamagnetic ($S = 0$) ^1H NMR spectrum (Figure S2), ruling out an $S = 1$ ground state for this complex. Photoreduction by the X-ray beam was also considered, but UV-vis spectra of crystals of **4** dissolved in ethyl acetate showed no change after X-ray irradiation (Figure S3).

We next considered a possible site disorder in the crystal lattice with an $Mn^{IV}(OH)(ttppc)$ impurity, which could be present from minor reduction of $Mn^V(O)$ during prolonged crystallization times. Magnetic susceptibility measurements (Figure S4) on crystalline **4** revealed the presence of a small amount of a paramagnetic species (16% Mn^{IV}), consistent with an $Mn^{IV}(OH)$ impurity. EPR analysis of crystalline **4** also revealed a weak signal indicative of the presence of a minor Mn^{IV} component (Figure S5). These data were consistent with a minor amount of $Mn^{IV}(OH)$ co-crystallizing with the $Mn^V(O)$ complex.

To determine if the amount of $Mn^{IV}(OH)$ impurity correlated with crystallization time, XRD data were collected on crystals of **4** isolated after standing in solution for 1 week (**4a**), 2 weeks, (**4a**), and one month (**4c**). The apparent lengthening of the Mn-O bond did indeed increase with longer crystallization times, as seen in Figure 5. Efforts to model the disorder of $Mn^V(O)$/ $Mn^{IV}(OH)$ were not successful due to the disorder of the Mn–O group above and below the corrole plane, as shown by the contoured Fourier maps in Figure S6. The observed elongation of the Mn–O bond distance in **4** most likely results from the averaging of the mixtures of the $Mn^V(O)$ and $Mn^{IV}(OH)$ bond distances in the crystal over time and space.

The single crystals that were used for the structure determinations of **4a-c** were each removed from the X-ray diffractometer immediately following data collection and dissolved in ethyl acetate for UV-vis spectroscopy. The intensity of the peak at 365 nm decreases in intensity relative to the 425 nm peak with crystallization time, as seen in Figure S7. These changes are consistent with an increase of the $Mn^{IV}(OH)$ impurity relative to $Mn^V(O)$ (ttppc), with the pure $Mn^{IV}(OH)$ complex exhibiting a single Soret band at 420 nm as seen in Figure 2. In fact, a linear correlation between the absorbance ratio (A_{365}/A_{425}) and the Mn-O bond distance is observed (Figure S8). The apparent bond elongation in **4** is similar to the bond elongations observed by Parkin for the Mo-O bond in $Mo(PMe_2Ph)_3OCl_2$, which arises from a compositional disorder *via* co-crystallization with the isostructural derivative $Mo(PMe_2Ph)_3Cl_3$, leading to unresolved site disorder of Mo-O/Mo-Cl groups with significantly different bond lengths.[70]

Further confirmation that the Mn^V–O bond distance is shorter than the apparent bond lengths seen in Figure 4 comes from resonance Raman (RR) spectroscopy. The Mn–O stretch for $Mn^V(O)(ttppc)$ in CH_2Cl_2 is $v(Mn–O) = 952$ cm^{-1}.[56] This vibration can be compared with other metal-oxo and related species in a Badger's rule plot,[71] which relates stretching frequency with bond distance. From the Badger's rule plot, normalized for

differences in atomic masses, an Mn–O distance of 1.59 Å is predicted for $Mn^V(O)(ttppc)$. This distance is in line with other $Mn^V(O)$ complexes, and is clearly shorter than the apparent distances seen by XRD in Figure 5. We conclude that **4** co-crystallizes with varying, small amounts of the isostructural $Mn^{IV}(OH)(ttppc)$ derivative, depending on crystallization time, and gives rise to an apparent elongated Mn^V–O bond distance due to a small amount of $Mn^{IV}(OH)$ in the crystals.

Synthesis and Structural Characterization of $Mn^{III}(H_2O)(ttppc)$.

Crystals of **1• H_2O** were grown from addition of a small amount of H_2O (50 μL) to a solution of **1** in fluorobenzene (1 mL), followed by removal of excess H_2O and slow vapor diffusion of *n*-pentane. Complex **1•H_2O** co-crystallizes with the metal-free corrole ($ttppcH_3$), which presumably forms during the crystallization process. The occupancy factor of the major component **1•H_2O** refines to 0.7114(15), and its structure is shown in Figure 6. The Mn–O bond distance in **1•H_2O** is 2.2645(18) Å and the two H atoms of the H_2O molecule were located from the difference Fourier maps (Figure S9). This Mn–O bond distance is also comparable to that reported for $Mn^{III}(H_2O)$ corrolazine (2.143(2) Å).[72] The structural characterization of **1•H_2O** completes the series of $Mn^V(O)$, $Mn^{IV}(OH)$, and $Mn^{III}(H_2O)$ complexes related by single H-atom transfer steps.

Density functional theory (DFT) calculations.

DFT calculations at the B3LYP/LANL2DZ/6–31G level of theory were performed on complexes **1•H_2O, 3**, and **4** to support the structural assignments. The DFT calculations were performed with starting structures that contained truncated forms of the triarylcorrole ligand, with the outer phenyl substituents removed from each of the *meso*-phenyl groups to facilitate the calculations. The experimental and calculated Mn–O, Mn–N_{ave}, and Mn–N_{plane} distances are given in Table 1.

The DFT-calculated Mn–O distances for both $Mn^{IV}(OH)(ttppc)$ and $Mn^{III}(H_2O)(ttppc)$ are in good agreement with those determined by single crystal XRD, as are the Mn–N_{ave} and Mn–N_{plane} distances. Complexes **1•H_2O** and **3** thus provide a good experimental calibration of our DFT methods. In contrast to **1•H_2O** and **3**, the DFT-derived Mn–O bond length for **4** (1.560 Å) deviates significantly from the experimentally obtained value (1.6332(16) Å), although it does fall in line with other structurally characterized $Mn^V(O)$ complexes.[65–68] The discrepancy for the $Mn^V(O)$ complex **4** further supports the conclusion that the apparent Mn–O bond length in **4** observed by single crystal XRD is elongated because of compositional disorder with a small amount of the $Mn^{IV}(OH)$ complex **3**.

H-atom Transfer Reactivity of $Mn^V(O)(ttppc)$ (4).

With the Mn complexes **1•H_2O, 3**, and **4** in hand, it is clear that the ttppc ligand provides an excellent platform for the isolation of manganese in three different oxidation states, together with sequential protonation at a terminal oxo ligand. The conversion from $Mn^V(O)$ (**4**) to $Mn^{IV}(OH)$ (**3**) to $Mn^{III}(H_2O)$ (**1•H_2O**) involves the formal transfer of hydrogen atoms. These complexes thus provide the rare opportunity to study sequential H-atom transfer (HAT) at a single terminal oxo ligand of a high-valent Mn, while holding the remaining ligands constant.

Initial attempts to study the HAT reactivity of **4** began with 9,10-dihydroanthracene (DHA), a common substrate employed to examine HAT reactions with high-valent metal-oxo complexes.[73–75] However, **4** reacts with DHA only very slowly (<5% reacted over 8 h). Slow kinetics for C-H cleavage were also seen with the related $Mn^V(O)$ corrolazine, which reacts with DHA with $k_2 = 1.8 \times 10^{-5}$ M^{-1} s^{-1}.[76] In contrast, it was found that complex **4** is capable of abstracting H atoms from aryl O-H bonds with relative ease. Addition of excess 2,4-di-*tert*-butylphenol (2,4-DTBP) to a solution of **4** in benzene at 23 °C caused complete isosbestic conversion of **4** (λ_{max} = 365, 425, 565 nm) to the Mn^{III}-aquo complex **1•H$_2$O** (λ_{max} = 412, 433, 660 nm) within 5 min (Figure 7a-b). Analysis of reaction mixtures by GC-FID revealed the formation of the phenol radical coupling product in 91(5) % yield (Figure S10), according to the stoichiometry shown in Figure 7a. The coupled dimer is the expected product following homolytic ArO-H bond cleavage, which initially should give a transient phenoxyl radical, and the $Mn^{IV}(OH)$ complex **2** after HAT. However, complex **2** was not detected, and only the Mn^{III} product was observed.

The kinetics of the reaction between **4** and 2,4-DTPB was monitored by UV-vis spectroscopy under pseudo-first-order conditions. Addition of excess 2,4-DTBP to **4** led to first-order decay of **4** and concomitant production of **1•H$_2$O,** as seen in Figure 7b. Satisfactory fits of the single-wavelength data (inset, Figure 7b) with a first-order rate expression gave pseudo-first-order rate constants (k_{obs}) that correlated linearly with substrate concentration (Figure 7c). The slope from Figure 7c gives a second-order rate constant of k_H = 17.4(1) M^{-1} s^{-1} for 2,4-DTBP. The deuterated phenol derivative, 2,4-DTBP(OD), was prepared and measured under the same conditions, giving k_D = 16.5(2) M^{-1} s^{-1}, and leading to a kinetic isotope effect (KIE) of k_H/k_D = 1.05 for ArO–H cleavage by **4**. The reactivity of **4** can be compared with $Mn^V(O)(tpfc)$ (tpfc = tris(pentafluorophenyl)corrole), which was examined by Abu-Omar and coworkers in reactions with 2,4-DTBP.[77] This complex oxidized 2,4-DTBP with k_2 = 45 M^{-1} s^{-1}, similar in magnitude to **4**. A KIE value of k_H/k_D = 1.3 was observed, which is larger than that seen for **4,** although still smaller than most other metal-oxo mediated HAT reactions.[76, 78–79] From product analysis, it is clear that **4** reacts with 2,4-DTBP *via* a net H-atom abstraction, although the small KIE suggests that the rate-determining step may not be a concerted HAT, and instead a mechanism closer to PCET may be operative.

The absence of the formation of $Mn^{IV}(OH)(ttppc)$ (**3**) in the reaction between **4** and 2,4-DTBP leads to two possible mechanisms (Scheme 2). The first mechanism (A) involves a $Mn^{IV}(OH)$ intermediate that is much more reactive as an H-atom abstractor than the starting $Mn^V(O)$ complex, giving a steady-state condition for $Mn^{IV}(OH)(ttppc)$. We have suggested a similar mechanism for the HAT reactivity of an analogous $Mn^V(O)$ corrolazine complex.[76] Alternatively, mechanism B involves rapid disproportionation of $Mn^{IV}(OH)(ttppc)$ to $Mn^V(O)(ttppc)$ and $Mn^{III}(H_2O)(ttppc)$, with the $Mn^V(O)$ complex serving as the sole oxidant in the system. These mechanistic possibilities for reactions mediated by high-valent metal-oxo corroles and porphyrins have been debated for some time.[1–4] The isolated $Mn^{IV}(OH)(ttppc)$ complex **2** provides a rare opportunity to address this mechanistic question by direct observation of the reactivity of the metal-hydroxide intermediate. In addition, the

general HAT reactivity of an $Mn^{IV}(OH)$ porphyrinoid complex is not known, and could be examined here for the first time.

$Mn^{IV}(OH)(ttppc)$ (3): a reactive HAT intermediate?

The reactivity of **3** with phenol derivatives was examined. Addition of excess 2,4-DTBP to **3** in benzene at 23 °C results in the rapid, isosbestic conversion of **3** to the Mn^{III} species **1·H$_2$O** (Figure 7e). Analysis by GC-FID revealed the formation of the bis(phenol) dimer in good yield (90(2)%), consistent with a single HAT to $Mn^{IV}(OH)$ to give the $Mn^{III}(H_2O)$ product. The rate of this reaction was measured by UV-vis spectroscopy, as done previously for **4**, and led to a second-order rate constant of $k = 2.73(12) \times 10^4$ M^{-1} s^{-1}. Comparison of the rate constant for the deuterated derivative of 2,4-DTBP gave a KIE = 1.40 for the abstraction of hydrogen by $Mn^{IV}(OH)$. Although this KIE is relatively small, it is similar to what is seen for $Mn^V(O)(tpfc)$,[77] and combined with our other data, it is reasonable to conclude HAT is the rate-determining step for this reaction.

The kinetic data clearly show that the $Mn^{IV}(OH)$ complex **3** reacts much more rapidly with phenol derivatives than the higher-valent $Mn^V(O)$ complex **4**. The HAT reaction with 2,4-DTBP occurs with a ~1570-fold rate increase, and points to mechanism A in Scheme 1. Further support for mechanism A comes from the stability of **3** in solution. There is no evidence of disproportionation of **3** (mechanism B) upon standing in C_6H_6 for hours, even over a wide range of concentrations (20 μM – 3 mM). We conclude that mechanism A is operative, and the $Mn^{IV}(OH)$ complex is a much more potent H-atom abstractor than the higher-valent $Mn^V(O)$ with O-H bonds.

While hydrogen atom transfer reactions have been widely studied for metal-oxo complexes, less is known about the hydrogen atom transfer reactivity of high-valent metal-hydroxo complexes. There are several reaction pathways by which net hydrogen atom transfer from phenols to **3** could occur; 1) electron transfer (ET) followed by proton transfer (PT), 2) PT followed by ET, or 3) concerted HAT. Kinetic studies were performed on a series of *para*-substituted 2,6-di-*tert*-butylphenol substrates (4-X-2,6-DTBP, X = OMe, Me, tBu, H) in benzene at 23 °C. Isosbestic conversion of **3** to **1** was observed upon addition of excess phenols, and a plot of the first order rate constant (k_{obs}) versus substrate concentration gave second order rate constants, ranging from $5.1(1) \times 10^2$ M^{-1}s^{-1} for the –OMe derivative to $36.3(1)$ M^{-1} s^{-1} for the –H derivative. Hammett analysis of the second order rate constants obtained from the reaction of **3** with 4-X-2,6-DTBP (Figure 8a) shows a decrease in the rate constants with an increase in the electron-withdrawing nature of the *para* substituent, giving $\rho^+ = -1.4(2)$, with good linearity ($r^2 = 0.975$). Slightly smaller ρ values were obtained for the H-atom abstraction of 4-X-2,6-DTBP by $Mn^V(O)$ corrolazine ($\rho^+ = -1.26$),[76] and of substituted phenols by $Fe^{IV}(O)(T2MPyP)$ (T2MPyP = tetra(2-*N*-methylpyridyl)porphyrin) ($\rho^+ = -1.10$),[81] which were indicative of a concerted H-atom transfer. A plot of log k vs. the bond dissociation energy (BDE) of the phenolic O-H bond (Figure S17) similarly gives a fairly linear correlation ($r^2 = 0.975$) with a slope of $-0.25(3)$. This linear relationship is indicative of an HAT mechanism,[82–83] however, due to the small BDE range (~4 kcal/mol) studied, care should be taken in interpreting this linearity.

Further support for a concerted H-atom transfer mechanism comes from a Marcus analysis of the second order rate constants for **3**. A linear free energy relationship between $(RT/F)\ln k$ vs. E_{ox} can be derived from the Marcus equation,[20, 84] wherein a slope of $\sim$$-0.5$ is expected for a simple rate-determining ET process. A plot of $(RT/F)\ln k$ vs. E_{ox} (k = second order rate constant, E_{ox} = redox potential of 4-X-2,6-DTBP derivative) affords a linear correlation with slope = $-0.12(1)$ (Figure 8b). This slope is much smaller than the expected -0.5 for a rate-limiting ET reaction, and is comparable to the slope (-0.05) for the reaction of cumylperoxyl radical and phenols, which is a clear example of concerted HAT.[85–86]

The reactivity of **3** toward the phenol derivatives can be compared with other high-valent metal-oxo and metal-hydroxo complexes (Table 2). The $Mn^{IV}(OH)$ complex **3** is by far the most reactive, oxidizing the phenols at rates that are 1–3 orders of magnitude greater than the other $Fe^{IV}(O)$, $Mn^{V}(O)$, and $Mn^{III}(OH)$ complexes in Table 2. Moreover, the Hammett slopes for the other complexes given in Table 2 are all negative, and relatively close to that obtained for **3**. These Hammett trends are consistent with only small charge separation in the transition state, and point to a concerted HAT mechanism as described for **3**. Thus, the increased reactivity for **3** is likely not due to a significant difference in the mechanism of phenol oxidation for **3** as compared to the other complexes in Table 2. Interestingly, the only other $Mn^{IV}(OH)$ complex in Table 2, $Mn^{IV}(OH)(salen)$, also exhibits good reactivity (at $-70\ ^{\circ}C$) with the same phenol substrates.[59]

The observed superior HAT reactivity of $Mn^{IV}(OH)(ttppc)$ compared to $Mn^{V}(O)(ttppc)$, as well as the other complexes in Table 2, deserves comment. The $Mn^{V}(O)$ complex might be expected to be a more reactive oxidant than the $Mn^{IV}(OH)$ complex based simply on oxidation state, and comparison of the oxidative reactivity of the few well characterized pairs of $M^{V}(O)/M^{IV}(O)$ complexes (M = Mn, Fe) agrees with this prediction.[87–89] The enhanced reactivity of **3** contrasts this trend, indicating that the obvious predictions based on oxidation state regarding HAT reactivity do not fit for the $Mn^{V}(O)/Mn^{IV}(OH)$ ttppc complexes. A comparison with the analogous heme enzyme intermediates $Fe^{IV}(O)$ $(porph^{\bullet+})/Fe^{IV}(OH)(porph)$, which are at the same relative oxidation levels and protonation states as **4** and **3**, is also informative. A direct comparison of the HAT reactivity of these species has recently been made for aromatic peroxygenase (APO), a thiolate-ligated heme enzyme.[90] In APO, protonated Cpd-II abstracts hydrogen from benzylic C-H bonds much more slowly than Cpd-I, consistent with the former species being a milder oxidant. Protonated Cpd-II is also generally less reactive than Cpd-I in the oxidation of phenolic O-H bonds, although the difference is much less apparent ($k_{(Cpd-I)} = 1.1$–$4.8 \times 10^7\ M^{-1}s^{-1}$ vs $k_{(protonated\ Cpd-II)} = 0.05 - 8.0 \times 10^7\ M^{-1}s^-$). Here again, the relative reactivity of the $Mn^{V}(O)/Mn^{IV}(OH)$ complexes appears to contradict these trends. Further investigations of **3** and **4** are warranted to determine the influence of other factors (e.g. spin state, redox potentials, proton affinities) on the HAT reactivity of these species.

SUMMARY AND CONCLUSIONS

The synthesis and characterization of a rare $Mn^{IV}(OH)$ complex ($Mn^{IV}(OH)(ttppc)$ (**3**)) was described, which is also the first example of a monohydroxo-Mn^{IV} complex to be characterized by XRD. The related $Mn^{V}(O)(ttppc)$ (**4**) and $Mn^{III}(H_2O)(ttppc)$ (**1•H$_2$O**)

complexes were prepared, completing a series of Mn complexes in three different oxidation states that could be interconverted by a single HAT within the same overall ligand environment. It was shown that **3** was capable of the facile oxidation of phenol derivatives, and kinetic analysis indicated that the mechanism of oxidation was best described as a concerted HAT mechanism. A key result obtained from these studies is the observation that the $Mn^{IV}(OH)$ complex **3** is a much more powerful oxidant toward phenol substrates than the higher-valent $Mn^V(O)$ complex **4**. This finding contradicts the expectation that the higher oxidation state complex should be the better oxidant, but falls in line with the observation that the $Mn^V(O)$ complex reacts with phenols *via* HAT to give $Mn^{III}(H_2O)$, without the observation of an $Mn^{IV}(OH)$ intermediate. These results help settle the debate regarding the mechanism of $Mn^V(O)$ oxidations in favor of Mechanism A in Scheme 2, which includes a highly reactive $Mn^{IV}(OH)$ intermediate. The $Mn^{IV}(OH)$ complex **3** is also a more powerful oxidant than $Fe^{IV}(O)$ complexes with the same series of phenol substrates, despite the fact that $Fe^{IV}(O)$ species are widely invoked as potent oxidants in synthetic catalysts and enzymes.

Water oxidation can be considered as the microscopic reverse of HAT to $Mn^V(O)$ to give $Mn^{III}(H_2O)$ (Scheme 1). The ability of $Mn^{IV}(OH)$ to rapidly abstract an H atom from phenols implies that the reverse concerted H-atom abstraction from an $Mn^{III}(H_2O)$ to give an $Mn^{IV}(OH)$ intermediate may be an unfavorable pathway in water oxidation. Thus separated proton/electron transfer steps, or multiproton/multielectron transfers, as opposed to a single, concerted HAT beginning with $Mn^{III}(H_2O)$, may be more favored for water oxidation by the Mn cluster in the OEC.

From the results presented here, it is clear that high-valent metal-hydroxide complexes can function as potent oxidizing species in their own right, in addition to the better known oxidants comprised of high-valent metal-oxo species. The nonheme enzyme SLO relies on such a species for C-H cleavage, and perhaps other enzymatic examples await discovery. In the meantime, the development of new high-valent metal-hydroxide species in synthetic models will allow for correlations to be made between their structural and electronic properties and their reactivity. Such work is ongoing in our laboratory.

EXPERIMENTAL SECTION

Materials.

All chemicals were purchased from commercial sources and used without further purification unless otherwise stated. Reactions involving inert atmosphere were performed under argon gas using standard Schlenk techniques or inside a nitrogen-filled dry box. Toluene, dichloromethane, acetonitrile, and diethyl ether were purified *via* a Pure-Solv solvent purification system from Innovative Technologies, Inc. 2,4-di-*tert*-butylphenol was recrystallized twice in *n*-pentane. The mono-deuterated 2,4-di-*tert*-butylphenol was prepared following a published procedure.[91] The phenol derivatives of formula 4-X-2,6-di-*tert*-butylphenol were purchased from Sigma-Aldrich, and then recrystallized twice in an appropriate solvent, ethanol (X = OMe, Me), acetonitrile (X = tBu) or *n*-pentane (X = H), and dried under vacuum. The metal-free ligand 5,10,15-tris(2,4,6-triphenylphenyl)corrole) (ttppcH$_3$) was synthesized following a modified procedure.[20] Iodosylbenzene (PhIO)

(>95%) was obtained from TCI chemicals. Deuterated solvents for NMR spectroscopy were purchased from Cambridge Isotopes, Inc.

Instrumentation.

UV-vis spectroscopy was performed on a Hewlett-Packard Agilent 8453 photodiode-array spectrophotometer. Samples were contained in a quartz cuvette (3. 5 mL, path length = 1 cm) fitted with a septum. UV-vis stopped-flow spectroscopy was carried out for reactions with total reaction times of less than ~10 seconds, using a HiTech SHU-61SX2 (TgK Scientific Ltd.) stopped-flow spectrophotometer with a xenon light source and Kinetic Studio software. Laser desorption ionization mass spectrometry (LDI-MS) was conducted on a Bruker Autoflex III MALDI ToF/ToF instrument (Billerica, MA) equipped with a nitrogen laser at 335 nm using an MTP 384 ground steel target plate. The instrument was calibrated using peptide standards of known molecular weights. Gas chromatography (GC-FID) was carried out on an Agilent 6850 gas chromatograph fitted with a DB–5 5% phenylmethyl siloxane capillary column (30 m x 0.32 mm x 0.25 μm) and equipped with a flame–ionization detector. ^{1}H NMR spectra were recorded on a Bruker Avance 400 MHz NMR spectrometer at 298 K, and referenced against residual solvent proton signals. Elemental analyses were performed at Atlantic Microlab, Inc., Norcross, GA. Electron paramagnetic resonance (EPR) spectra were recorded with a Bruker EMX spectrometer equipped with a Bruker ER 041 X G microwave bridge and a continuous-flow liquid helium cryostat (ESR900) coupled to an Oxford Instruments TC503 temperature controller for low temperature data collection. Cyclic voltammetry was performed on an EG&G Princeton Applied Research potentiostat/galvanostat model 263A with a three-electrode system consisting of a glassy carbon working electrode, a Ag/AgNO$_3$ non-aqueous reference electrode (0.01 M AgNO$_3$ with 0.1 M Bu$_4$NPF$_6$ in CH$_3$CN), and a platinum wire counter electrode. Potentials were referenced using an external ferrocene standard. Scans were run under an Ar atmosphere at 23 ˚C using Bu$_4$NPF$_6$ (0.1 M) as the supporting electrolyte.

Synthesis of Mn^{III}(H$_2$O)(ttppc) (1•H$_2$O).

Complex **1** was synthesized by metalation of ttppcH$_3$ with Mn(OAc)$_2$ • 4 H$_2$O following a published procedure.[56] After purification of **1** by column chromatography in Et$_2$O/basic alumina, the H$_2$O-bound complex **1 H$_2$O** was synthesized by addition of a small amount of distilled H$_2$O (50 μL) to **1** dissolved in fluorobenzene (1 mL) followed by stirring for 2 h. After manually separating the excess water, vapor diffusion of *n*-pentane led to the slow formation of dark green crystals of Mn^{III}(H$_2$O)(ttppc) (**1 H$_2$O**) after 2 weeks.

Synthesis of Mn^{IV}(Cl)(ttppc) (2).

A solution of **1** (0.250 g, 0.198 mmol) in CH$_2$Cl$_2$ (100 mL) was stirred with aqueous HCl (100 mL, 1.0 M) for 1 h. The organic layer was washed with water (3 × 50 mL), and dried over anhydrous Na$_2$SO$_4$. The solvent was removed, and the residue was purified by column chromatography on silica gel (4:1 CH$_2$Cl$_2$/hexanes, R_f = 0.40) to obtain **2** as a pure brown solid (0.103 g, 40% yield). The relatively low yield was due to the dematalation of **1**, giving ttppcH$_3$ which was recovered as a green solid (R_f = 0.74). Crystals of **2** suitable for XRD were obtained by layering a CH$_2$Cl$_2$ solution of **2** with *n*-hexane, followed by slow

evaporation of this mixture over 1 week. This method gave **2** as dark brown blocks. UV-vis (benzene): λ_{max}, nm (ε x 10^{-4} M^{-1} cm^{-1}): 420 (2.95), 460 (2.64), 710 (0.25). LDI-MS (m/z): isotopic cluster centered at 1263.4 (M-Cl$^+$) (calcd 1263.4). Anal. Calcd for $C_{91}H_{59}MnN_4Cl$: C, 84.15; H, 4.58; N, 4.31. Found: C, 84.79; H, 4.89; N, 4.33.

Synthesis of Mn^{IV}(OH)(ttppc) (3).

To a dark brown solution of **2** (20.0 mg, 15.4 μmol) in toluene (5 mL) was added an aqueous solution of LiOH (5 mL, 5% w/v), and the biphasic mixture was stirred for 1 h. Completion of the reaction was observed by UV-vis spectroscopy. The toluene layer was extracted, washed with water (3 × 5 mL), and dried over anhydrous sodium sulfate. The brown solution was then passed through a short plug of Celite and dried *in vacuo* to give **3** as a dark brown solid. Crystals of **3** suitable for XRD were obtained by vapor diffusion of *n*-pentane into toluene over 1 week under anaerobic conditions, giving **3** as brown blocks (12.6 mg, 64% yield). UV-vis (benzene): λ_{max}, nm (ε x 10^{-4} M^{-1} cm^{-1}): 420 (3.62) LDI-MS (m/z): isotopic cluster centered at 1280.6 (M$^+$) (calcd 1280.4). Anal. Calcd for $C_{91}H_{60}MnON_4$: C, 85.36; H, 4.72; N, 4.38. Found: C, 84.45; H, 4.86; N, 4.26.

Synthesis of Mn^{V}(O)(ttppc) (4).

The complex was synthesized following a modification of a published procedure.[56] To a solution of **1** (70 mg, 55.4 μmol) in ethyl acetate (5 mL) was added PhIO (120 mg, 0.55 mM), and the solution was stirred for 5 min, after which a color change from green to red was observed. The solution was passed through a short plug of basic alumina to remove unreacted PhIO. Vapor diffusion of this solution with *n*-pentane gave **4** as dark-red blocks (17 mg, 24% yield) after 1 week (**4a**). For crystals of **4** with variable crystallization time, crystals were grown in ethyl acetate/*n*-pentane for 2 weeks (**4b**), or in benzene/*n*-heptane for 1 month (**4c**). UV-vis (benzene): λ_{max}, nm (ε x 10^{-4} M^{-1} cm^{-1}): 365 (3.30), 425 (4.20), 565 (0.81) ^{1}H NMR (400 MHz, C_6D_6) δ (ppm): 8.71 (d, *J* = 4.5 Hz, 2H), 8.49 (dt, *J* = 14.5, 4.9 Hz, 6H), 8.20 – 8.10 (m, 6H), 7.80 (dt, *J* = 6.6 Hz, 6H), 7.38 (td, *J* = 7.4, 3.2 Hz, 6H), 7.33 – 7.24 (m, 3H), 7.07 (d, *J* = 7.5 Hz, 4H), 6.94 (d, *J* = 7.5 Hz, 4H), 6.90 (d, *J* = 7.4 Hz, 2H), 6.82 (d, *J* = 7.4 Hz, 2H), 6.53 – 6.12 (m, 18H), LDI-MS (m/z): isotopic cluster centered at 1279.5 (M$^+$) (calcd 1279.4). Anal. Calcd for $C_{91}H_{59}MnN_4O$: C, 85.43; H, 4.65; N, 4.38. Found: C, 85.39; H, 4.79; N, 4.33.

Reaction of 3 with 2,4-di-*tert*-butylphenol. Product analysis.

To a solution of **3** in benzene (500 μL, 3.3 mM) was added 2,4-di-*tert*-butylphenol (10 μmol, 6 equiv) and the internal standard eicosane (6 mM). The reaction was monitored by UV-vis spectroscopy, which showed complete conversion of **3** to **1**. The reaction mixture was directly injected onto the GC for analysis. The phenol oxidation product 3,3',5,5'-tetra-*tert*-butyl-(1,1'-biphenyl)-2,2'-diol was identified by GC in comparison with an authentic sample, and quantified by integration of the peak and comparison with a calibration curve constructed with an internal standard (eicosane). The reaction was performed in triplicate. Average yield = 90(2)% based on the reaction stoichiometry of 0.5 equiv phenol oxidation product per 1.0 equiv of **3**.

Reaction of 4 with 2,4-di-*tert*-butylphenol. Product analysis.

To a solution of **4** in benzene (500 μL, 3.3 mM) was added 2,4-di-*tert*-butylphenol (16.5 μmol, 10 equiv) and the internal standard eicosane (6 mM). The reaction was monitored by UV-vis spectroscopy, which showed complete conversion of **4** to **1**. The reaction mixture was directly injected onto the GC for analysis. The phenol oxidation product 3,3',5,5'-tetra-*tert*-butyl-(1,1'-biphenyl)-2,2'-diol was identified by GC in comparison with an authentic sample, and quantified by integration of the peak and comparison with a calibration curve constructed with an internal standard (eicosane). The reaction was performed in triplicate. Average yield = 91(5)% based on the reaction stoichiometry of 1.0 equiv phenol oxidation product per 1.0 equiv of **4**.

Kinetic studies. Reaction of Mn^V(O)(ttppc) with 2,4-di-*tert*-butylphenol.

To a benzene solution of Mn^V(O)(ttppc) **(4)** (2 mL, 15 μM) at 23 °C, varying amounts of 2,4-di-*tert*-butylphenol or mono-deuterated 2,4-di-*tert*-butylphenol (0.5 – 2.8 mM) were added to start the reaction. The spectral changes showed isosbestic conversion of **4** (λ = 365, 425, 565 nm) to **1** (λ = 412, 433, 660 nm). The pseudo-first-order rate constants, k_{obs}, for these reactions were obtained by non-linear least-squares fitting of the plots of absorbance at 365 or 660 nm (Abs$_t$) versus time (t) according to the equation Abs$_t$ = Abs$_f$ + (Abs$_0$ – Abs$_f$) exp(–k$_{obs}$t), where Abs$_0$ and Abs$_f$ are the initial and final absorbance, respectively. Second order rate constants, k_2 (M^{-1}s^{-1}) were obtained from the slope of the best-fit line from a plot of k_{obs} (s^{-1}) vs 2,4-di-*tert*-butyl phenol concentration (M).

Kinetic studies. Reaction of Mn^{IV}(OH)(ttppc) with 2,4-di-*tert*-butylphenol, and 4-X-2,6-DTBP derivatives.

In a typical reaction, Mn^{IV}(OH)(ttppc) **(3)** (15 μM) was reacted with varying amounts of 2,4-di-*tert*-butylphenol, mono-deuterated 2,4-di-*tert*-butylphenol (0.4 – 1.7 mM), or 4-X-2,6-DTBP (X = OMe, Me, tBu, H) in benzene at 23 °C. The spectral changes showed isosbestic conversion of **3** (λ = 420 nm) to **1** (λ = 412, 433, 660 nm). The same kinetic analysis was used as employed for kinetic studies with **4**, following the growth in absorbance at 660 nm corresponding to production of **1**. Plot of the resulting k_{obs} (s^{-1}) values versus substrate concentration (M) were linear and yielded second order rate constants, k_2 (M^{-1}s^{-1}).

Computational Methods.

Calculations on the manganese complexes ^{1}[Mn^V(O)(tpc)], ^{4}[Mn^{IV}(OH)(tpc)] and ^{5}[Mn^{III}(H$_2$O)(tpc)] (tpc = 5,10,15-triphenylcorrole) utilized density functional theory (DFT) as implemented in the *Orca* program package.[92] Geometry optimizations and frequency calculations were performed using the unrestricted hybrid density functional B3LYP with the LANL2DZ[93] basis set on Mn and the 6–31G[94] basis set on the remaining atoms. The initial geometries of the manganese complexes were obtained from the X-ray crystal structures of the complexes, with the 2,4,6-triphenyl substituents on each *meso*-phenyl group replaced with hydrogen atoms. Independent calculations have shown that the addition of electron-donating substituents, or sterically bulky groups, to the meso-phenyl groups does not affect the Mn–O bond distances for the manganese complexes discussed. Optimized

geometries were used for frequency calculations at the same level of theory to ensure the local minimum nature of the geometry (without any imaginary frequencies).

Supplementary Material

Refer to Web version on PubMed Central for supplementary material.

ACKNOWLEDGMENT

REFERENCES

(1). Zhang R; Horner JH; Newcomb M, J. Am. Chem. Soc 2005, 127, 6573.15869278,

(2). Fukuzumi S; Fujioka N; Kotani H; Ohkubo K; Lee Y-M; Nam W, J. Am. Chem. Soc 2009, 131, 17127.19888722,

(3). Kumar A; Goldberg I; Botoshansky M; Buchman Y; Gross Z, J. Am. Chem. Soc 2010, 132, 15233.20932015,

(4). Pan Z; Newcomb M, Inorg. Chem 2007, 46, 6767.17630728,

(5). Baglia RA; Zaragoza JPT; Goldberg DP, Chem. Rev 2017, 117, 13320.28991451,

(6). Engelmann X; Monte-Pérez I; Ray K, Angew. Chem. Int. Ed 2016, 55, 7632.,

(7). Nam W; Lee Y-M; Fukuzumi S, Acc. Chem. Res 2014, 47, 1146.24524675,

(8). McDonald AR; Que L, Coord. Chem. Rev 2013, 257, 414.,

(9). Sahu S; Goldberg DP, J. Am. Chem. Soc 2016, 138, 11410.27576170,

(10). Taguchi T; Stone KL; Gupta R; Kaiser-Lassalle B; Yano J; Hendrich MP; Borovik AS, Chem. Sci 2014, 5, 3064.25580212,

(11). Gao H; Groves JT, J. Am. Chem. Soc 2017, 139, 3938.28245648,

(12). Brines LM; Coggins MK; Poon PCY; Toledo S; Kaminsky W; Kirk ML; Kovacs JA, J. Am. Chem. Soc 2015, 137, 2253.25611075,

(13). Ching W-M; Zhou A; Klein JEMN; Fan R; Knizia G; Cramer CJ; Guo Y; Que L, Inorg. Chem 2017, 56, 11129.28858496,

(14). Donoghue PJ; Tehranchi J; Cramer CJ; Sarangi R; Solomon EI; Tolman WB, J. Am. Chem. Soc 2011, 133, 17602.22004091,

(15). Porter TR; Mayer JM, Chem. Sci 2014, 5, 372.24729854,

(16). Wijeratne GB; Corzine B; Day VW; Jackson TA, Inorg. Chem 2014, 53, 7622.25010596,

(17). Coggins MK; Brines LM; Kovacs JA, Inorg. Chem 2013, 52, 12383.24156315,

(18). Goldsmith CR; Cole AP; Stack TDP, J. Am. Chem. Soc 2005, 127, 9904.15998097,

(19). Yosca TH; Rittle J; Krest CM; Onderko EL; Silakov A; Calixto JC; Behan RK; Green MT, Science 2013, 342, 825.24233717,

(20). Zaragoza JPT; Yosca TH; Siegler MA; Moënne-Loccoz P; Green MT; Goldberg DP, J. Am. Chem. Soc 2017, 139, 13640.28930448,

(21). Yin G; McCormick JM; Buchalova M; Danby AM; Rodgers K; Day VW; Smith K; Perkins CM; Kitko D; Carter JD; Scheper WM; Busch DH, Inorg. Chem 2006, 45, 8052.16999402,

(22). Kurahashi T; Kikuchi A; Tosha T; Shiro Y; Kitagawa T; Fujii H, Inorg. Chem 2008, 47, 1674.18237118,

(23). Ortiz de Montellano PR, Chem. Rev 2010, 110, 932.19769330,

(24). Poulos TL, Chem. Rev 2014, 114, 3919.24400737,

(25). Rittle J; Green MT, Science 2010, 330, 933.21071661,

(26). Huang X; Groves JT, J. Biol. Inorg. Chem 2017, 22, 185.27909920,

(27). Makris TM; von Koenig K; Schlichting I; Sligar SG, J. Inorg. Biochem 2006, 100, 507.16510191,

(28). Denisov IG; Makris TM; Sligar SG; Schlichting I, Chem. Rev 2005, 105, 2253.15941214,

(29). Rettie AE; Sheffels PR; Korzekwa KR; Gonzalez FJ; Philpot RM; Baillie TA, Biochemistry 1995, 34, 7889.7794900,

(30). Rettie AE; Boberg M; Rettenmeier AW; Baillie TA, J. Biol. Chem 1988, 263, 13733.3138238,

(31). Rettie AE; Rettenmeier AW; Howald WN; Baillie TA, Science 1987, 235, 890.3101178,

(32). Hsieh CH; Huang X; Amaya JA; Rutland CD; Keys CL; Groves JT; Austin RN; Makris TM, Biochemistry 2017, 56, 3347.28603981,

(33). Grant JL; Mitchell ME; Makris TM, Proc. Natl. Acad. Sci 2016, 113, 10049.27555591,

(34). Zachos I. Ga; Bauer D; Sieber V; Hollmann F; Kourist R, Chem. Commun 2015, 51, 1918.,

(35). Dennig A; Kuhn M; Tassoti S; Thiessenhusen A; Gilch S; Bülter T; Haas T; Hall M; Faber K, Angew. Chem. Int. Ed 2015, 54, 8819.,

(36). Klinman JP; Offenbacher AR; Hu S, J. Am. Chem. Soc 2017, 139, 18409.29244501,

(37). Offenbacher AR; Hu S; Poss EM; Carr CAM; Scouras AD; Prigozhin DM; Iavarone AT; Palla A; Alber T; Fraser JS; Klinman JP, ACS Cent. Sci 2017, 3, 570.28691068,

(38). Klinman JP, Biochemistry 2013, 52, 2068.23373460,

(39). Yano J; Yachandra V, Chem. Rev 2014, 114, 4175.24684576,

(40). Umena Y; Kawakami K; Shen J-R; Kamiya N, Nature 2011, 473, 55.21499260,

(41). Dau H; Zaharieva I; Haumann M, Curr. Opin. Chem. Biol 2012, 16, 3.22387134,

(42). Cox N; Retegan M; Neese F; Pantazis DA; Boussac A; Lubitz W, Science 2014, 345, 804.25124437,

(43). Rapatskiy L; Cox N; Savitsky A; Ames WM; Sander J; Nowaczyk MM; Rögner M; Boussac A; Neese F; Messinger J; Lubitz W, J. Am. Chem. Soc 2012, 134, 16619.22937979,

(44). Lassalle-Kaiser B; Hureau C; Pantazis DA; Pushkar Y; Guillot R; Yachandra VK; Yano J; Neese F; Anxolabehere-Mallart E, Energy Environ. Sci 2010, 3, 924.24772190,

(45). Rivalta I; Brudvig GW; Batista VS, Curr. Opin. Chem. Biol 2012, 16, 11.22481113,

(46). Gupta R; Taguchi T; Lassalle-Kaiser B; Bominaar EL; Yano J; Hendrich MP; Borovik AS, Proc. Natl. Acad. Sci 2015, 112, 5319.25852147,

(47). Kanady JS; Tsui EY; Day MW; Agapie T, Science 2011, 333, 733.21817047,

(48). Mukherjee S; Stull JA; Yano J; Stamatatos TC; Pringouri K; Stich TA; Abboud KA; Britt RD; Yachandra VK; Christou G, Proc. Natl. Acad. Sci 2012, 109, 2257.22308383,

(49). Vaddypally S; Kondaveeti SK; Karki S; Van Vliet MM; Levis RJ; Zdilla MJ, J. Am. Chem. Soc 2017, 139, 4675.28288514,

(50). Zhang C; Chen C; Dong H; Shen J-R; Dau H; Zhao J, Science 2015, 348, 690.25954008,

(51). Schwarz B; Forster J; Goetz MK; Yücel D; Berger C; Jacob T; Streb C, Angew. Chem. Int. Ed 2016, 55, 6329.,

(52). Pal S; Chan MK; Armstrong WH, J. Am. Chem. Soc 1992, 114, 6398.,

(53). Garcia-Bosch I; Company A; Cady CW; Styring S; Browne WR; Ribas X; Costas M, Angew. Chem. Int. Ed 2011, 50, 5648.,

(54). For $Mn^{IV}(OH)$ complexes characterized by X-ray absorption spectroscopy, see Refs. 10 and 22.

(55). Fukuzumi S; Kotani H; Prokop KA; Goldberg DP, J. Am. Chem. Soc 2011, 133, 1859.21218824,

(56). Liu H-Y; Yam F; Xie Y-T; Li X-Y; Chang CK, J. Am. Chem. Soc 2009, 131, 12890.19737012,

(57). Golubkov G; Bendix J; Gray HB; Mahammed A; Goldberg I; DiBilio AJ; Gross Z, Angew. Chem. Int. Ed 2001, 40, 2132.,

(58). Ou Z; Erben C; Autret M; Will S; Rosen D; Lex J; Vogel E; Kadish KM, J. Porphyrins Phthalocyanines 2005, 09, 398.,

(59). Kurahashi T; Kikuchi A; Shiro Y; Hada M; Fujii H, Inorg. Chem 2010, 49, 6664.20553024,

(60). Zdilla MJ; Dexheimer JL; Abu-Omar MM, J. Am. Chem. Soc 2007, 129, 11505.17718564,

(61). Charnock JM; Garner CD; Trautwein AX; Bill E; Winkler H; Ayougou K; Mandon D; Weiss R, Angew. Chem., Int. Ed 1995, 34, 343.,

(62). Leto DF; Ingram R; Day VW; Jackson TA, Chem. Commun 2013, 49, 5378.,

(63). Chen J; Lee Y-M; Davis KM; Wu X; Seo MS; Cho K-B; Yoon H; Park YJ; Fukuzumi S; Pushkar YN; Nam W, J. Am. Chem. Soc 2013, 135, 6388.23324100,

(64). Wu X; Seo MS; Davis KM; Lee Y-M; Chen J; Cho K-B; Pushkar YN; Nam W, J. Am. Chem. Soc 2011, 133, 20088.22091637,

(65). Baglia RA; Prokop-Prigge KA; Neu HM; Siegler MA; Goldberg DP, J. Am. Chem. Soc 2015, 137, 10874.26295412,

(66). MacDonnell FM; Fackler NLP; Stern C; O'Halloran TV, J. Am. Chem. Soc 1994, 116, 7431.,

(67). Collins TJ; Gordon-Wylie SW, J. Am. Chem. Soc 1989, 111, 4511.,

(68). Hong S; Lee Y-M; Sankaralingam M; Vardhaman AK; Park YJ; Cho K-B; Ogura T; Sarangi R; Fukuzumi S; Nam W, J. Am. Chem. Soc 2016, 138, 8523.27310336,

(69). Zhao H; Pierloot K; Langner EHG; Swarts JC; Conradie J; Ghosh A, Inorg. Chem 2012, 51, 4002.22432719,

(70). Yoon K; Parkin G; Rheingold AL, J. Am. Chem. Soc 1992, 114, 2210.,

(71). Spaeth AD; Gagnon NL; Dhar D; Yee GM; Tolman WB, J. Am. Chem. Soc 2017, 139, 4477.28319386,

(72). Neu HM; Jung J; Baglia RA; Siegler MA; Ohkubo K; Fukuzumi S; Goldberg DP, J. Am. Chem. Soc 2015, 137, 4614.25839905,

(73). Klein JEMN; Dereli B; Que L; Cramer CJ, Chem. Commun 2016, 52, 10509.,

(74). Cho K; Leeladee P; McGown AJ; DeBeer S; Goldberg DP, J. Am. Chem. Soc 2012, 134, 7392.22489757,

(75). Baglia RA; Krest CM; Yang T; Leeladee P; Goldberg DP, Inorg. Chem 2016, 55, 10800.27689821,

(76). Lansky DE; Goldberg DP, Inorg. Chem 2006, 45, 5119.16780334,

(77). Bougher CJ; Liu S; Hicks SD; Abu-Omar MM, J. Am. Chem. Soc 2015, 137, 14481.26517943,

(78). Cho J; Woo J; Eun Han J; Kubo M; Ogura T; Nam W, Chem. Sci 2011, 2, 2057.,

(79). Hohenberger J; Ray K; Meyer K, Nat. Commun 2012, 3, 720.22395611,

(80). Sastri CV; Lee J; Oh K; Lee YJ; Lee J; Jackson TA; Ray K; Hirao H; Shin W; Halfen JA; Kim J; Que L; Shaik S; Nam W, Proc. Natl. Acad. Sci 2007, 104, 19181.18048327,

(81). Colclough N; Smith JRL, J. Chem. Soc., Perkin Trans 2 1994, 1139.,

(82). Mayer JM, Acc. Chem. Res 2011, 44, 36.20977224,

(83). Mayer JM, Annu. Rev. Phys. Chem 2004, 55, 363.15117257,

(84). Marcus RA; Sutin N, Biochim. Biophys. Acta, Rev. Bioenerg 1985, 811, 265.,

(85). Lee JY; Peterson RL; Ohkubo K; Garcia-Bosch I; Himes RA; Woertink J; Moore CD; Solomon EI; Fukuzumi S; Karlin KD, J. Am. Chem. Soc 2014, 136, 9925.24953129,

(86). Osako T; Ohkubo K; Taki M; Tachi Y; Fukuzumi S; Itoh S, J. Am. Chem. Soc 2003, 125, 11027.12952484,

(87). Pattanayak S; Jasniewski AJ; Rana A; Draksharapu A; Singh KK; Weitz A; Hendrich M; Que L; Dey A; Sen Gupta S, Inorg. Chem 2017, 56, 6352.28481521,

(88). Arunkumar C; Lee Y-M; Lee JY; Fukuzumi S; Nam W, Chem. – Eur. J 2009, 15, 11482.19810056,

(89). Jeong YJ; Kang Y; Han A-R; Lee Y-M; Kotani H; Fukuzumi S; Nam W, Angew. Chem. Int. Ed 2008, 47, 7321.,

(90). Wang X; Ullrich R; Hofrichter M; Groves JT, Proc. Natl. Acad. Sci 2015, 112, 3686.25759437,

(91). Kundu S; Miceli E; Farquhar ER; Ray K, Dalton Trans 2014, 43, 4264.24362244,

(92). Neese F, WIREs: Comput. Mol. Sci 2012, 2, 73.,

(93). Hay PJ; Wadt WR, J. Chem. Phys 1985, 82, 299.,

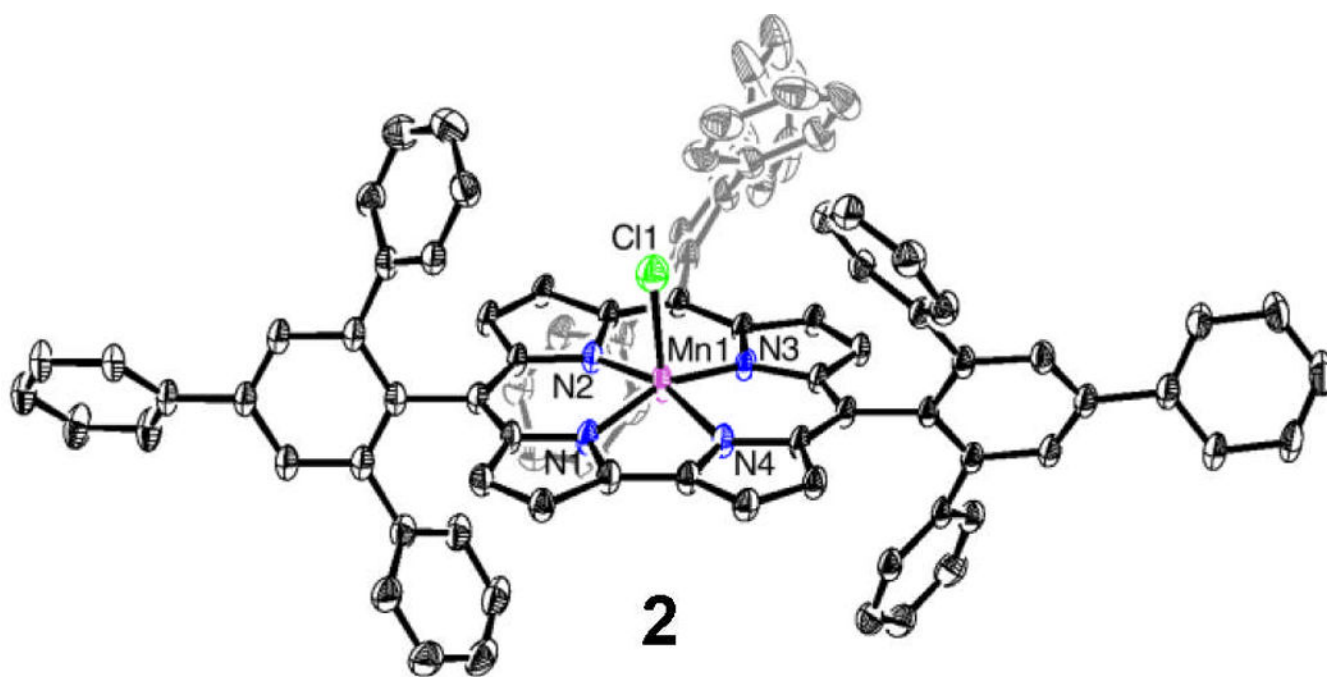(94). Hehre WJ; Ditchfield R; Pople JA, J. Chem. Phys 1972, 56, 2257.,

Figure 1.
Displacement ellipsoid plots (35% probability level) for Mn^{IV}(Cl)(ttppc) (**2**) at 110(2) K. Hydrogen atoms omitted for clarity.
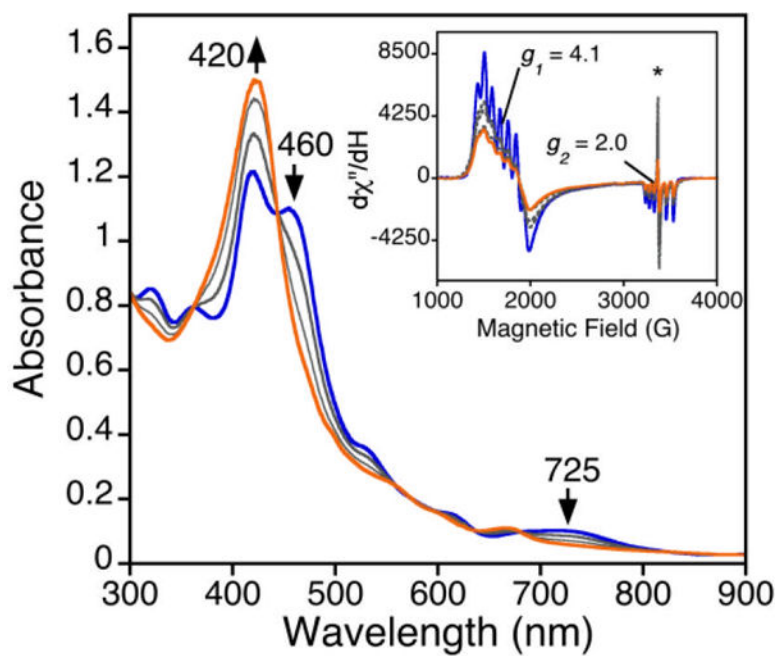
Figure 2.
UV-vis spectral titration of **2** with NBu$_4$OH (0, 0.33, 0.66, 1.0 equiv) in toluene/CH$_3$CN (100:1 v/v) at 23 °C. Inset: changes in the X-band EPR spectra of **2** (blue line) upon titration with Bu$_4$NOH (0 – 1.0 equiv) in toluene/CH$_3$CN (4:1 v/v) at 12 K (final spectrum, orange line). (* = radical impurity ($S = \frac{1}{2}$)).
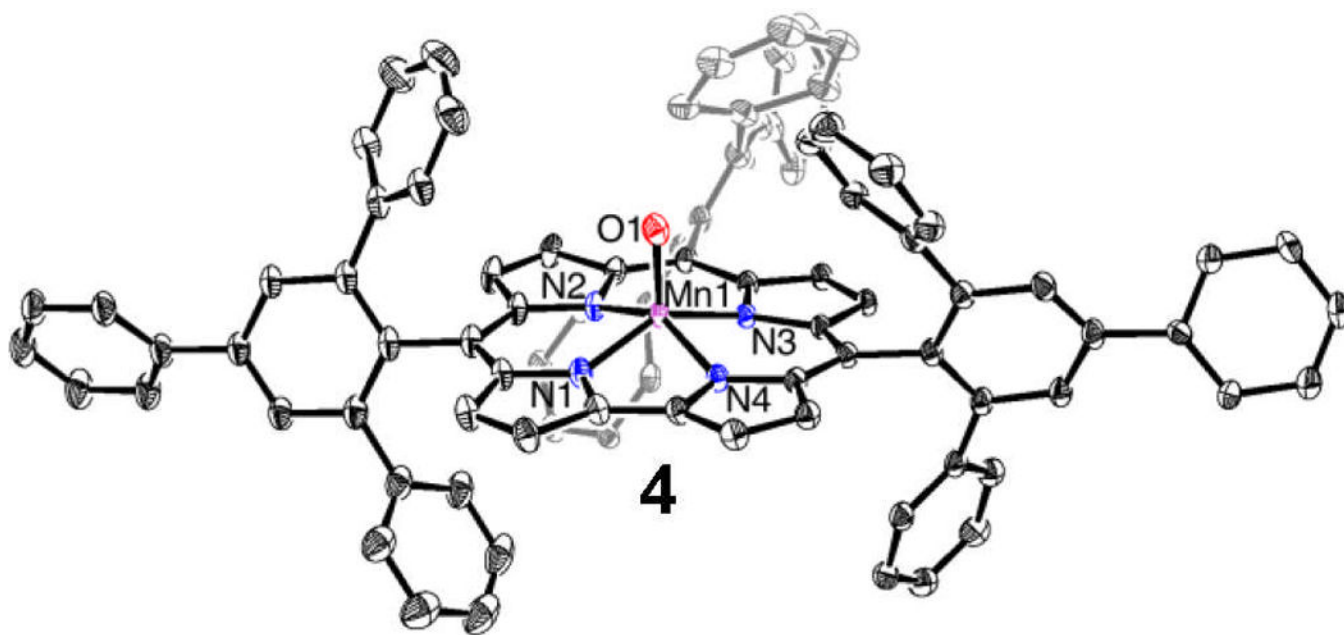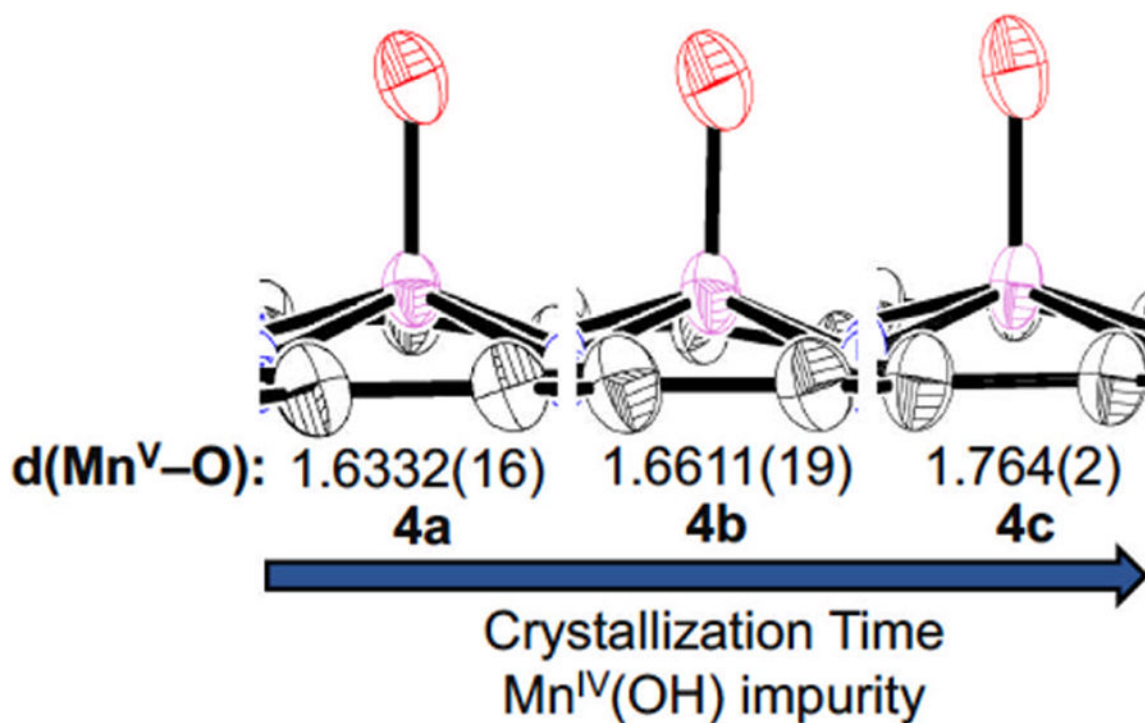
Figure 3.
Displacement ellipsoid plot (35% probability level) for $Mn^{IV}(OH)(ttppc)$ (**3**) at 110(2) K.
Hydrogen atoms (except H1) omitted for clarity.

Figure 4.
Displacement ellipsoid plot (35% probability level) for $Mn^V(O)(ttppc)$ (**4**) at 110(2) K. H atoms omitted for clarity.

d(Mn^V–O): 1.6332(16) 1.6611(19) 1.764(2)

4a **4b** **4c**

Crystallization Time

Mn^{IV}(OH) impurity

Figure 5.
Displacement ellipsoid plots (50% probability level) for the Mn–O unit in **4** at 110(2) K, from crystals grown over different time periods. The structures were obtained from crystals of **4** grown for 1 week (**4a**), 2 weeks (**4b**), and 1 month (**4c**). All bond distances are given for the major component of the Mn–O group which is disordered over two positions (~7:3 occupancy) above and below the plane of the corrole.
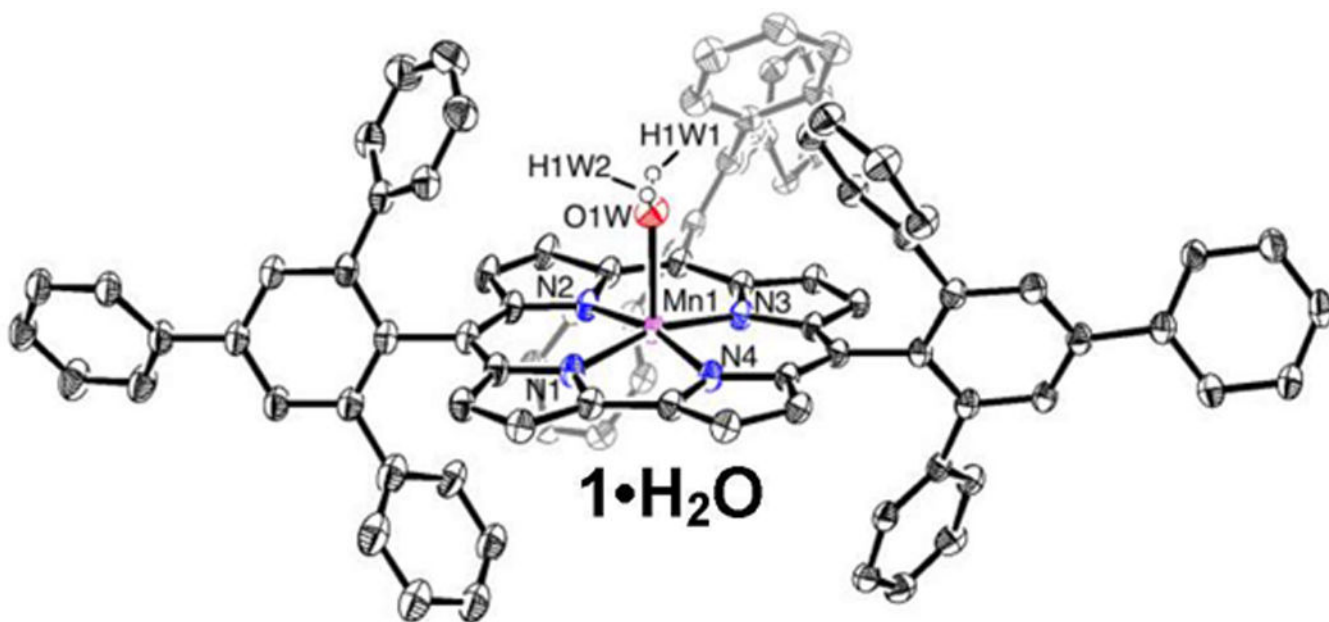
Figure 6.
Displacement ellipsoid plot (35% probability level) for $Mn^{III}(H_2O)(ttppc)$ ($\mathbf{1 \cdot H_2O}$) at 110(2) K. H atoms (except for those attached to O) omitted for clarity.
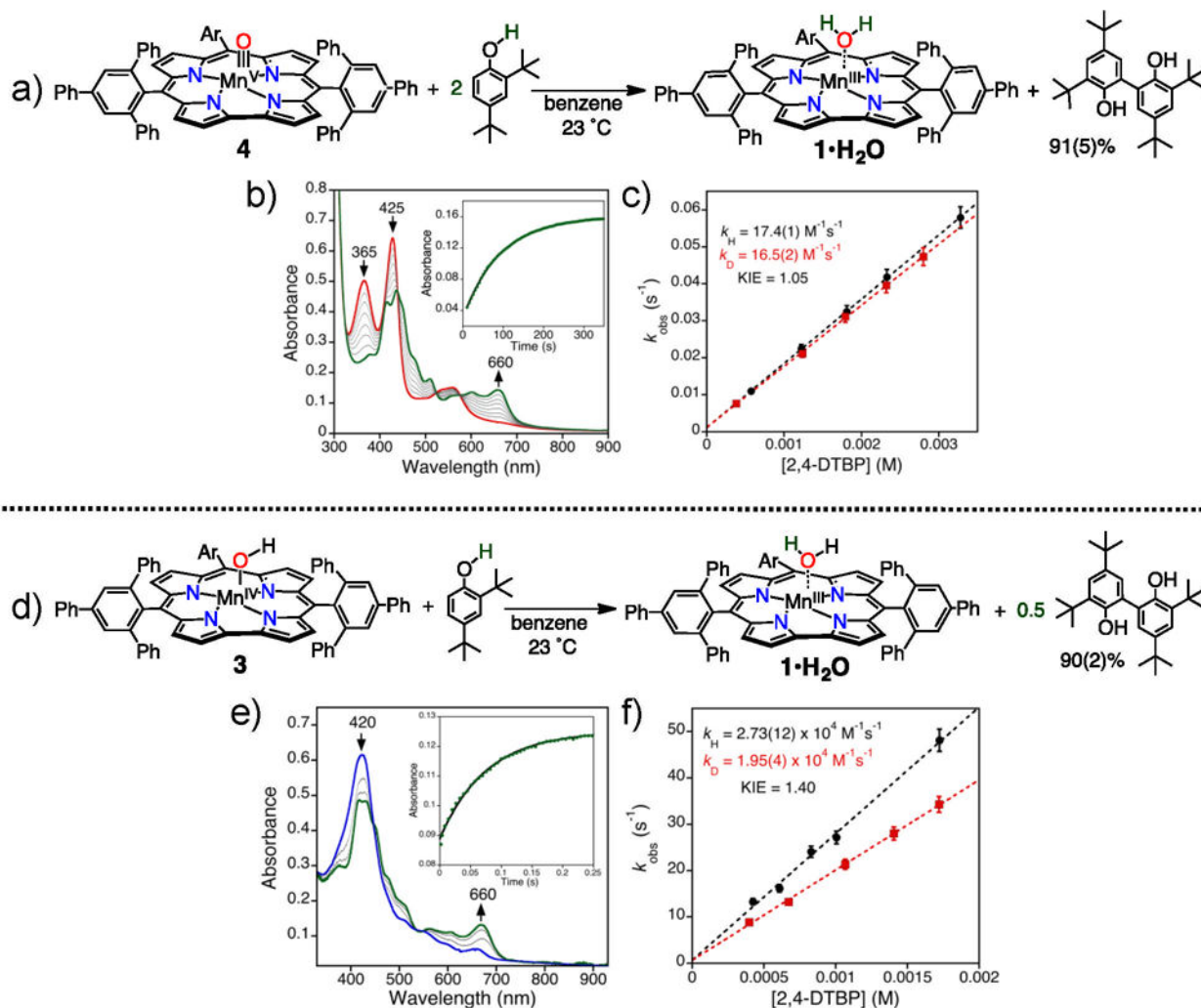
Figure 7.

a) Reaction of $Mn^V(O)$(ttppc) (**4**) and 2,4-DTBP. b) Time-resolved UV−vis spectral changes for the reaction between (**4**) (15 μM) and 2,4-DTBP (0.5 mM) in benzene at 23 °C. Inset: change in absorbance vs time for the growth of Mn^{III}(ttppc) (660 nm) (green circles) with the best fit line (black). c) Plot of pseudo-first order rate constants (k_{obs}) versus [2,4-DTBP-OH] (black circles) and [2,4-DTBP-OD] (red squares). d) Reaction of $Mn^{IV}(OH)$(ttppc) (**3**) and 2,4-DTBP. e) Time-resolved UV−vis spectral changes for the reaction between (**3**) (15 μM) and 2,4-DTBP (0.42 mM) in benzene at 23 °C. Inset: change in absorbance vs time for the growth of Mn^{III}(ttppc) (660 nm) (green circles) with the best fit line (black). f) Plot of pseudo-first order rate constants (k_{obs}) versus [2,4-DTBP-OH] (black circles) and [2,4-DTBP-OD] (red squares).
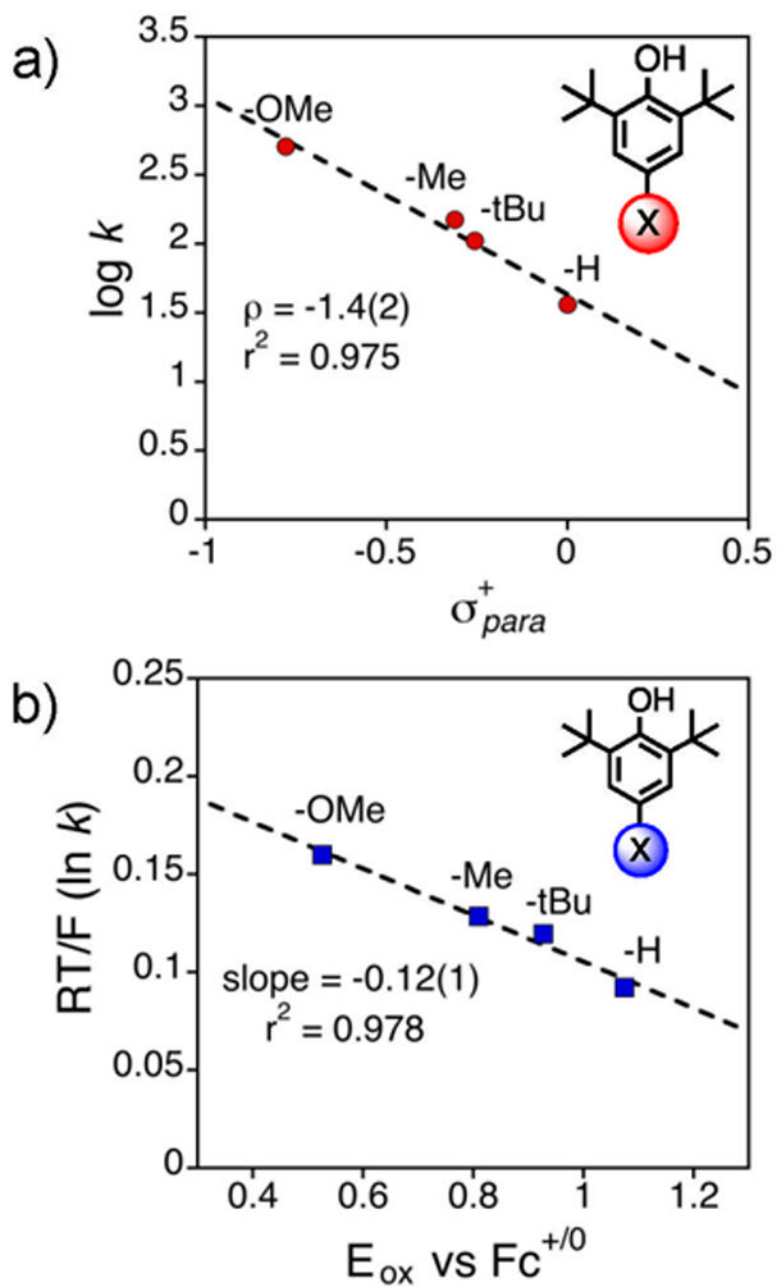
Figure 8.
Hammett (a) and Marcus (b) plots for the reaction of $Mn^{IV}(OH)(ttppc)$ (**3**) and 4-X-2,6-DTBP (X = -OMe, -Me, -tBu, -H) in benzene at 23 °C.
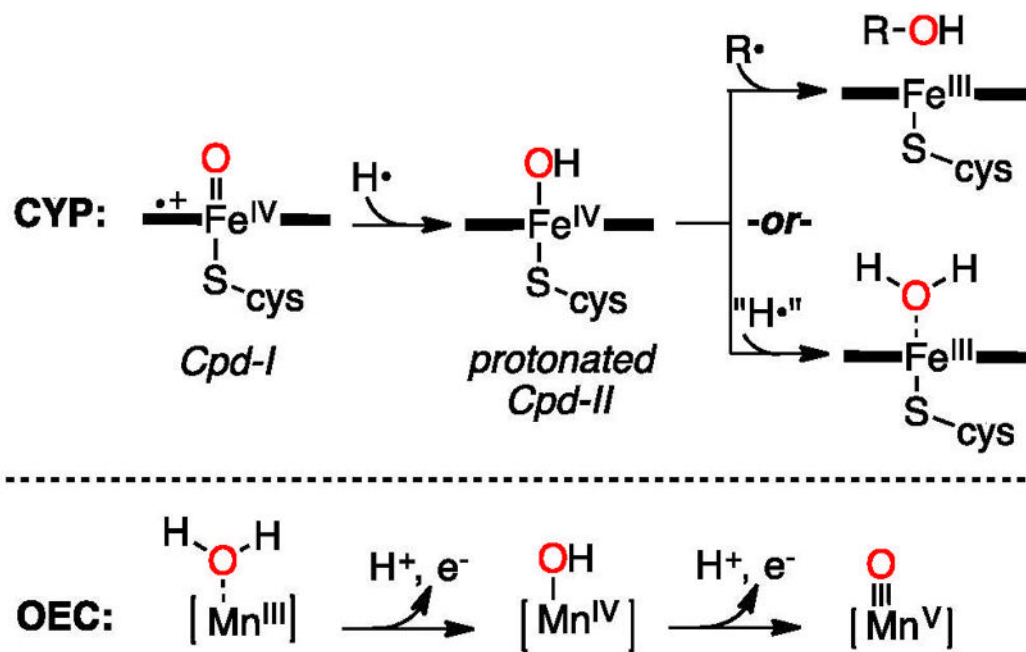
Scheme 1.
Net H-atom Transfers in the Active Sites of CYP and OEC
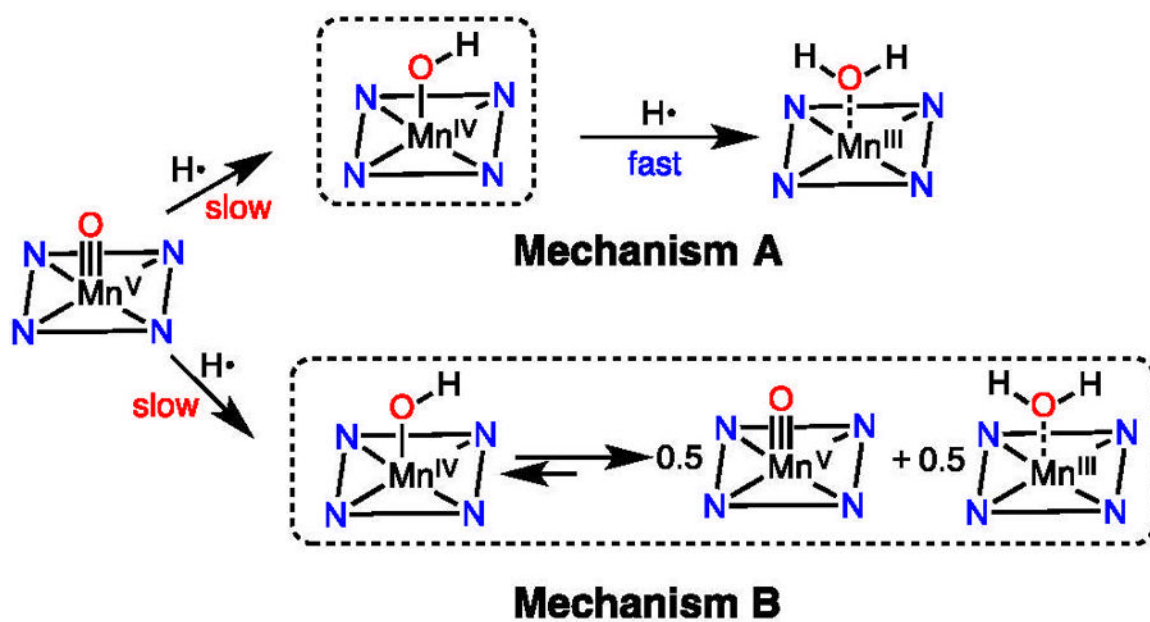
Scheme 2.
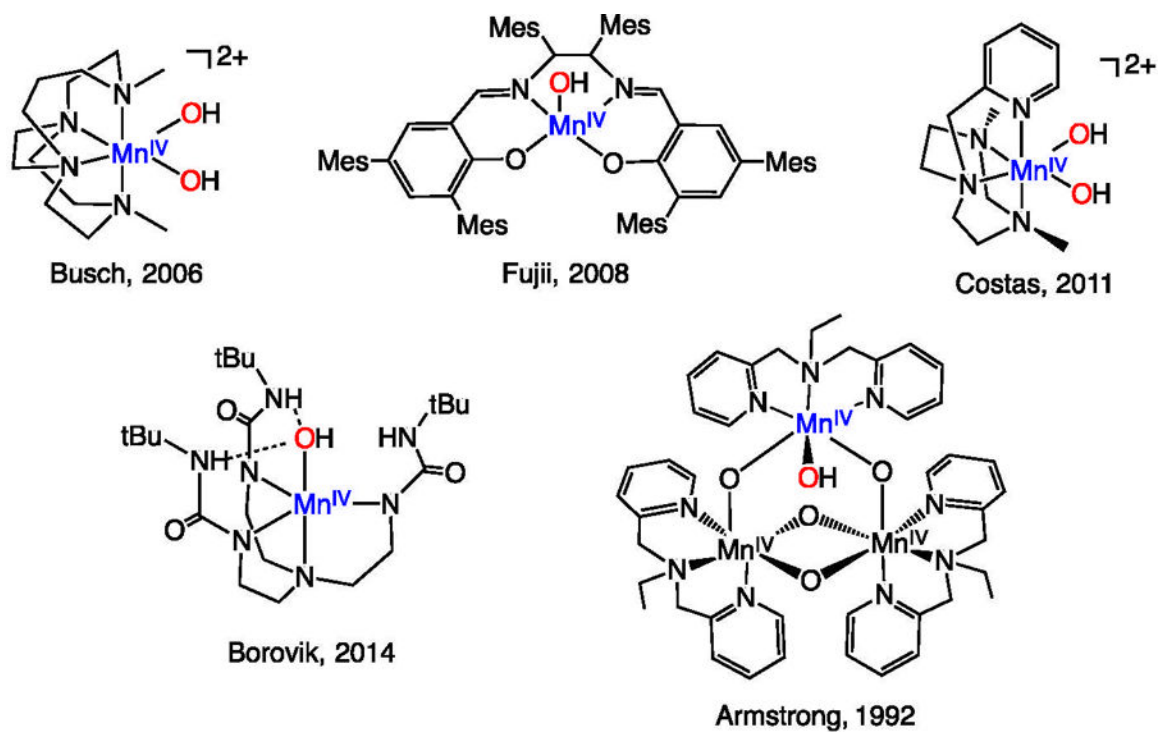Possible Mechanisms for H-atom Abstraction by an $Mn^V(O)$ Complex

Chart 1.
Examples of $Mn^{IV}(OH)_n$ (n = 1, 2) Complexes

Table 1.

Comparison of Select Experimental and Calculated Metrical Parameters for 1•H_2O, 3, and 4.

	$Mn^V(O)(ttppc)$ (4)		$Mn^{IV}(OH)(ttppc)$ (3)		$Mn^{III}(H_2O)(ttppc)$ (1•H_2O)	
	X-ray	**DFT**	**X-ray**	**DFT**	**X-ray**	**DFT**
Mn–O	1.6332(16)	1.560	1.881(2)	1.867	2.2645(18)	2.254
Mn–N$_{ave}$	1.9093(12)	1.916	1.9051(14)	1.941	1.9077(14)	1.922
Mn–N$_{plane}$	0.527	0.535	0.372	0.408	0.218	0.196

Table 2.

Comparison of second order rate constants (M^{-1} s^{-1}) for the oxidation of the phenol derivatives 4-X-2,6-DTBP (X = OMe, Me, tBu, H) by M(O) and M(OH) complexes.

4-X-DTBP	–OMe	–Me	–tBu	–H	ρ^+	Conditions
$Mn^{IV}(OH)(ttppc)$ (**3**)	510	150	105	36	−1.4	benzene, 23 ˚C
$Mn^{III}(OH)(dpaq)^+$ [a]	1.44	1.20	0.96	0.75	−0.88	CH_3CN, 50 ˚C
$Mn^V(O)(TBP_8Cz)$ [b]	0.45	0.02	0.01	0.008	−1.26	CH_2Cl_2, 25 ˚C
$Fe^{IV}(O)(TMC)(NCCH_3)^+$ [c]	11.4	0.18	0.22	0.04	−3.20	CH_3CN, 25 ˚C
$Fe^{IV}(O)(TMC)(CF_3COO)$ [c]	26.4	1.84	0.90	0.46	−2.30	CH_3CN, 25 ˚C
$Fe^{IV}(O)(TMC)(N_3)$ [c]	29.8	1.84	1.02	0.68	−1.50	CH_3CN, 25 ˚C
$Mn^{IV}(OH)(salen)$ [d]	nd	0.02	0.007	0.002	nd	CH_2Cl_2, −70 ˚C

[a] from Ref. 16, calculated from reported k_{obs} (s^{-1}) values.

[b] from Ref. 76.

[c] from Ref. 80, calculated from reported k_{obs} (s^{-1}) values.

[d] from Ref. 59.